Sensors and Materials, Vol. 37, No. 6 (2025) 2325–2349
MYU Tokyo

S & M 4058

Fault Diagnosis of Gear Lubrication Systems Using Sensor Measurements and Data-driven Machine Learning: A Case Study of a Nuclear Power Plant

Wenjuan Zhang, Kun-Chieh Wang,* Hao Gao, and Yu Mao

School of Mechanical and Electric Engineering, Sanming University, Sanming 365004, Fujian Province, China

(Received January 27, 2025; accepted May 13, 2025)

Keywords: gear lubrication system, nuclear power plant, online monitoring, fault diagnosis, adaptive sparse principal component analysis

To address the issue that the fault diagnosis of the gear lubrication system of a nuclear power plant primarily relies on expert knowledge and experience, leading to numerous nuclear accidents, we propose an innovative integrated data-driven machine learning (IDDML) method based on sensor measurements. This IDDML method consists of two major components. The first is the fault tree analysis, which uses fault trees to identify critical fault paths and calculate failure probabilities. The second is the adaptive sparse principal component analysis based on variable projection combined with proximal gradient optimization (VPPGO-ASPCA) method. This method incorporates a modified principal component analysis technique and an optimization algorithm with an adaptive threshold. Compared with traditional diagnostic methods used in gear failure detection, our proposed IDDML method offers higher detection accuracy and improved sensitivity. Additionally, to compare and validate our proposed method, we developed a unique real-time measurement system that integrates multiple high-sensitivity sensors and employs four network architectures for the fault diagnosis of the gear lubrication system in a nuclear power plant. Experimental and computational results demonstrate that the IDDML fault diagnosis method achieves a fault detection success rate of up to 99%.

1. Introduction

The intricacies of the power gear lubrication system of nuclear power plants make it particularly challenging for operators to monitor and diagnose anomalies in real time. Currently, there are three mainstream methods for the fault diagnosis of such complex systems: model-driven, knowledge-driven, and data-driven.[1] The advantage of a model-driven method lies in its ability to provide an in-depth understanding of the system. By simulating its behavior through physical and chemical principles, the system ensures the reliability and accuracy of the predictive model.[2] The model-driven approach is particularly effective in situations where large amounts of historical data are unavailable, as it can derive key parameters from known system characteristics. Song *et al.* [3] simulated a steam generator pipe rupture accident and concluded

*Corresponding author: e-mail: m18316252102@126.com
https://doi.org/10.18494/SAM5571

ISSN 0914-4935
https://myukk.org/

that a data-driven approach can make accurate and rapid diagnostic predictions. Gong *et al.*[4] investigated nuclear reactor physics problems and employed a model-driven method to predict the core neutron distribution. Further investigation revealed that there has been almost no unified model-driven approach for diagnosing and predicting physical issues in recent years. This is because constructing models in a model-driven method is not only expensive but also demands a substantial amount of theoretical and experimental data.[5] Therefore, scholars are currently integrating model-driven methods with other approaches to leverage complementary advantages and offer more comprehensive and precise solutions. The knowledge-driven fault diagnosis method is an expert system approach that integrates principles from expert experience, knowledge bases, and inference machines. Knowledge-driven methods encompass if-then rules, symbolic directed graphs, Bayesian networks, dynamic uncertain causal graphs, and more. Wu *et al.*[6] introduced a fault diagnosis method tailored for distributed nuclear power plants. They employed back-propagation neural networks and decision trees for inference, integrating these methods with collected data for comprehensive global diagnosis. Their research findings demonstrate that their method achieves high diagnostic reliability and accuracy. Zhao *et al.*[7] introduced an artificial reasoning system based on Bayesian networks to estimate the conditional probabilities of equipment failure conditions in nuclear power plants. Domain knowledge was sourced from experts and the literature. This inference system demonstrates high diagnostic accuracy, particularly in failure scenarios involving motor-driven centrifugal pumps and cooling tower fan operations. However, the probabilistic method used in this approach relies on a fixed type of function, making it non-adaptable and time-consuming to calculate.[8] Wu *et al.*[9] proposed a method for the monitoring and fault diagnosis of electromechanical parts in nuclear power plants based on directed symbolic graphs. This inference method, which integrates process monitoring with qualitative trend analysis and a five-level threshold approach, can effectively improve the accuracy of fault detection and diagnosis. However, the knowledge-driven method heavily relies on specialized knowledge and experience in model building. Furthermore, determining the priori probability remains an unsolved problem.

With the advancement of data mining technologies such as machine learning, artificial intelligence, and pattern recognition, along with the abundance of operational data provided by digital measurement systems, the data-driven method has become the latest research hotspot in the field of fault diagnosis. Farber and Cole[10] proposed a method that combines artificial neural networks with particle filters to detect small-scale water loss incidents (SSWLIs) in pressurized water reactors. This method combines the data-driven and model-driven approaches to detect SSWLIs in real time and estimate their impact range. Wang *et al.*[11] proposed a fault identification and diagnosis method based on kernel principal component analysis and similarity clustering schemes for nuclear power plant equipment. At the same time, Li *et al.*[12] used principal component analysis (PCA) to monitor the electrical components of real nuclear power plants under various operating conditions. Chao *et al.*[13] proposed an end-to-end deep learning network method, in which the algorithm uses heterogeneous convolution kernels to automatically extract transient features from detected data and predict the future state of the nuclear power system. In the above research, scholars collected multivariable data during the operation of electromechanical systems for fault diagnosis. When the acquired data are univariable, such as speed or vibration signals, artificial intelligence schemes are typically employed for the complementary preprocessing of the signal data to improve the accuracy and efficiency of fault diagnosis. Ling *et al.*[14] proposed a fault prediction method that integrates probabilistic PCA and recurrent neural network schemes. Ren *et al.*[15] proposed a joint fault diagnosis model based on the sparse matrix scheme in conjunction with the support vector machine (SVM) scheme. Currently, the fault diagnosis methods for the gear lubrication system of a nuclear power plant primarily utilize data-driven methods. Pawashe *et al.*[16] measured the dielectric constant to determine the quality of lubricating oil in the lubrication system of a nuclear power plant in real time, including parameters such as acid value, iron content, water content, and density. They proposed an accurate oil change time to avoid engine damage and reduce oil costs. Ren *et al.*[17] introduced the Bayesian network method combined with expert knowledge and historical data to accurately diagnose fault conditions in a diesel lubrication system. Wang *et al.*[18] proposed a fault diagnosis method based on an SVM model and centroid positioning algorithm, which was used to diagnose two typical faults in a diesel lubrication system. Wang *et al.*[19] studied the sensor layout of an engine lubrication system and proposed an innovative condition monitoring method. Liu *et al.*[20] developed a fault diagnosis technology that combines the backpropagation neural network scheme with the information fusion method for fault detection in the hydraulic drive servo system of a rocket launcher.

Regarding the inspection of power gear lubrication systems of a nuclear power plant, no data-driven method has yet been proposed for fault diagnosis. Currently, fault diagnosis for these systems primarily relies on simple threshold judgment methods or expert knowledge. These approaches often lead to subjective errors and lack the generalization ability necessary for effective fault diagnosis. Additionally, although data-driven methods can address these issues, the variety of fault types in the lubrication system, the limited data available, and the unknown prior probabilities prevent timely fault diagnosis. To overcome these problems, we propose an integrated fault diagnosis method. First, the fault tree method is used to analyze the fault types in the power gear lubrication system of a nuclear power plant. Then, a data-driven machine learning algorithm is introduced to diagnose the faults. Finally, we validate the proposed method both theoretically and experimentally through four network schemes, using failure cases from the gear lubrication system of a nuclear power plant as a case study.

2. Innovative Integrated Data-driven Machine Learning (IDDML) Method

The IDDML method consists of two major components. The first is the fault tree analysis (FTA), which uses fault trees to identify critical fault paths and calculate failure probabilities. The second is the adaptive sparse PCA based on variable projection combined with proximal gradient optimization (VPPGO-ASPCA) method.

2.1 FTA

FTA is a system engineering analysis tool that reveals and qualitatively and quantitatively evaluates, through logical graphical patterns, the failure factors that lead to system failure. This approach uses logical symbols such as “AND” and “OR” to effectively map the various possible sources of failure to their effects, so that we can understand the possible paths of failure of the system.[21] The steps of FTA are shown in Fig. 1 and described as follows.

Step 1: Define top events.
Step 2: Define and identify middle and basic events.
Step 3: Construct fault trees.
Step 4: Optimize fault trees.
Step 5: Qualifying and quantifying analysis of faults.
Step 6: Identify weakness of failure parts.
Step 7: Make plans for fault diagnosis and prevention.

2.2 Fault detection method

2.2.1 PCA

The PCA method can be widely used in fields such as process monitoring, information extraction, computer vision, image processing, and fault detection owing to its powerful capabilities in dimensionality reduction and feature extraction.[22] The principle of PCA is to reduce the dimensionality of data while maximizing the retention of the original data information by identifying the main components and extracting the key features, which are detailed as follows: In the field of fault detection research, we typically process the data of a system using the T^2 and Q statistics to determine whether the system is faulty. The first step is to normalize a given data matrix $x \in R^{m \times n}$ as follows:

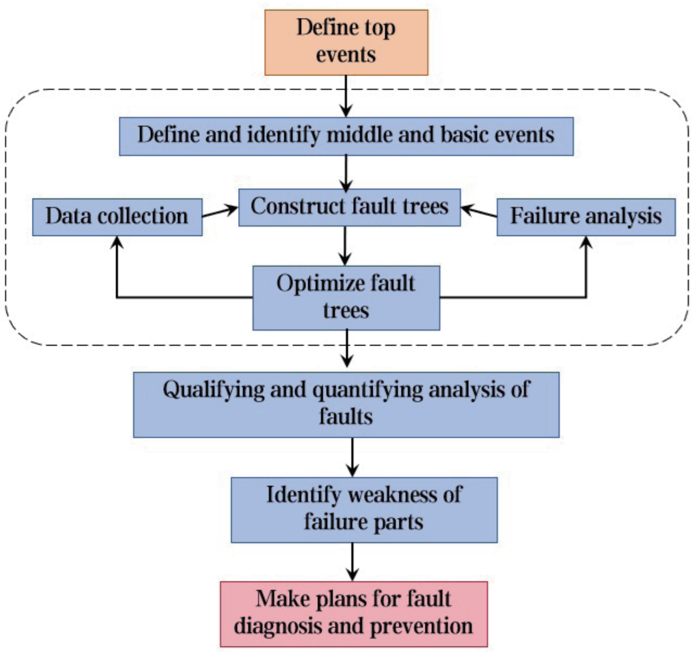

Fig. 1. (Color online) Steps of FTA.

$$X = \frac{x - \overline{x}}{s}, \tag{1}$$

$$\overline{x} = \frac{1}{n}\sum_{j=1}^{n} x_j, \tag{2}$$

$$s = \sqrt{\frac{1}{n-1}\sum_{j=1}^{n}(x_j - \overline{x})^2}, \tag{3}$$

where n is the sample number and X is the normalized data of x. The eigenvalue decomposition of the data matrix X yields

$$\mathrm{cov}(X) = \frac{X^T X}{m-1} = V\Lambda V^T, \tag{4}$$

where $V \in R^{n\times n}$ is the eigenvector matrix with load vector as its row elements and $\Lambda \in R^{n\times n}$ is a diagonal matrix with eigenvalues as its diagonal elements. We select the first k largest eigenvalues and their corresponding eigenvectors to construct a load matrix $P \in R^{n\times k}$. Now projecting the data of P onto the principal component space, we obtain the component matrix T as

$$T = XP. \tag{5}$$

The cumulative percentage contribution of the *kth* principal component of T can be found using the equation

$$CPV(k) = \frac{\Sigma_{i=1}^{k}\lambda_i}{\Sigma_{i=1}^{n}\lambda_i} \times 100\%. \tag{6}$$

The residual matrix is defined as

$$E = X - TP^T. \tag{7}$$

For the ith observation, its T^2 statistic is defined as

$$T_i^2 = x_i^T P\Lambda^{-1}P^T x_i. \tag{8}$$

For the ith observation, its Q statistic is defined as

$$Q_i = e_i^T e_i = x_i^T (I - PP^T)x_i, \tag{9}$$

where x_i is the observation vector of the dataset at the ith moment and e_i is the residual vector of x_i. The fixed threshold for T^2 based on the chi-square distribution is calculated from

$$T_\xi^2 = \frac{k(n^2-1)}{n(n-k)} F_\alpha(k, n-k), \tag{10}$$

where n is the number of training samples, k is the number of principal components, and $F_\alpha(k, n-k)$ is the α quantile of F distribution for the degree of freedom k and $n-k$. The fixed threshold of Q is

$$Q_\xi = \theta_1 \left(\frac{c_\alpha \sqrt{2\theta_2 {h_0}^2}}{\theta_1} + 1 + \frac{\theta_2 h_0 (h_0 - 1)}{\theta_1^2} \right)^{1/h_0}, \tag{11}$$

where c_α denotes the critical value at which the chi-square distribution reaches a significant level, θ_1 and θ_2 are the parameters that define the residual variance, and h_0 is an adustable factor that is typically related to the dimensions of the data and the selected principal fraction. The method of setting a fixed threshold for the Q statistic, as described above, assumes that the sample data follows a multivariate normal distribution. If the sample data does not follow a multivariate normal distribution, an empirical approach is used to determine the fixed threshold of the Q statistic. In this case, the threshold for a given confidence level is determined on the basis of the actual distribution of the data.(23)

The threshold T_ξ^2 with respect to the α percentile of dataset T^2 is calculated as

$$T_\xi^2 = T^2_{\left(\left\lceil \frac{\alpha}{100} n \right\rceil\right)}. \tag{12}$$

The threshold Q_ξ with respect to the α percentile of dataset Q is calculated as

$$Q_\xi = Q_\xi = Q_{\left(\left\lceil \frac{\alpha}{100} n \right\rceil\right)}, \tag{13}$$

where n is the observation number of T^2 and Q in the dataset and $\lceil \cdot \rceil$ indicates rounding up. In practical data analysis, since $\frac{\alpha}{100} n$ may not be an integer, it is often necessary to interpolate T_ξ^2 and Q_ξ. If z is the integer part of D and g is the decimal part, T_ξ^2 and Q_ξ can be estimated using the following interpolation formula:

$$T_\xi^2 = T_{(z)}^2 + g \cdot (T_{(z+1)}^2 - T_{(z)}^2), \tag{14}$$

$$Q_\xi = Q_{(z)} + g \cdot \left(Q_{(z+1)} - Q_{(z)} \right). \tag{15}$$

After setting the thresholds for the specific statistics of T_i and Q_i, we implement the following measures to detect anomalies in the process. At each time point, we calculate the statistics of T_i and Q_i from the collected data and compare them with the predetermined thresholds. If any statistic exceeds its corresponding threshold at a given time point, it can be inferred that there is an anomaly in the process.

2.2.2 Sparse PCA (SPCA)

In SPCA, the principal components are sparse linear combinations of few selected features, meaning they are primarily affected by a small number of variables, while the contributions of others are zero. This characteristic is particularly valuable in high-dimensional data analysis, where PCA typically produces principal components that are linear combinations of all original variables. In such high-dimensional settings, interpreting the physical meaning of principal components can be challenging. SPCA, however, helps identify the most significant features, making the principal components easier to interpret and understand.(24–27) The detailed descriptions about the SPCA method are as follows.(28)

First, we calculate the total variance from

$$Total\_Var = \sum_{j=1}^{m} \frac{1}{n-1} \sum_{i=1}^{n} (X_{ij} - \mu_j)^2 , \tag{16}$$

where X_{ij} is the element of the data matrix X and μ_j is the mean of the elements in the jth row obtained from

$$\mu_i = \frac{1}{n} \sum_{i=1}^{n} X_{ij} . \tag{17}$$

For every principal component V_i, i = 1, 2, ..., k, the element X_i and the variance of the principal component, *Var,* are calculated from

$$X_i = X \cdot V_i (V_i^T \cdot V_i)^{-1} V_i^T , \tag{18}$$

$$Var_i = \sum_{j=1}^{n} (X_i^T \cdot X_i)_{jj} , \tag{19}$$

where $X_i^T \cdot X_i$ means the inner product of X_i. The cumulative contribution of the kth principal component is

$$CPV(k) = \frac{\Sigma_{i=1}^{k} Var_i}{Total\_\mathrm{var}} \times 100\% . \tag{20}$$

Therefore, the number of principal components can be determined when the cumulative contribution reaches 85% or more.

From Eqs. (5)–(7), we have

$$X = E + XPP^T. \tag{21}$$

Then, we can finally build the SPCA model in the form of a regression problem as

$$(\hat{A}, \hat{B}) = \underset{A,B}{\arg\min} \left\| X - XAB^T \right\|^2 + \lambda \left\| B \right\|^2. \tag{22}$$

When $A = B$, the above equation becomes a traditional PCA model. In Eq. (22), $AA^T = I$ where I is a unit matrix, B is the expected load vector, and A is a middle matrix during iteration. Then, the load vector in the SPCA model is converted to a sparse load vector by constraining the load with the Lasso regression algorithm as

$$(\hat{A}, \hat{B}) = \underset{A,B}{\arg\min} \left\| X - XAB^T \right\|^2 + \lambda_1 \left\| B \right\|^2 + \lambda_2 \left\| B \right\|_1. \tag{23}$$

After solving the above equation, the final T^2 and Q statistics can be calculated using Eqs. (8)–(15).

2.2.3 VPPGO-ASPCA(29)

- Stochastic initialization

First, we perform a low-rank approximation of X to obtain $\tilde{X}$, and then we carry out a singular value decomposition of $\tilde{X}$:

$$\tilde{X} = UDV^T. \tag{24}$$

- Variable projection combined with proximal gradient algorithm

Considering the function

$$F(A,B) = G(A, H(B)), \tag{25}$$

we initially set A and B as the load matrix P, which is composed of the elements from the right singular matrix V in Eq. (24). Then, we construct a minimization problem as

$$\underset{A,B}{\text{minimize}}\, f(A,B) = \frac{1}{2} \left\| \tilde{X} - \tilde{X}BA^{\mathrm{T}} \right\|_F^2 + \alpha \left\| B \right\|_1 + \frac{1}{2}\beta \left\| B \right\|_F^2, \tag{26}$$

where $A^TA = I$, $\|\bullet\|_F$ is the Frobenius norm, $\|\bullet\|_1$ is the L_1 norm, α is the tuning parameter used to control sparsity, β is the regularization factor used to prevent overfitting, A is the scoring matrix, and B is a sparse load. Equation (26) can be simplified as

$$v(B) = \arg\min_{A} \| \tilde{X} - \tilde{X}BA^{\mathrm{T}} \|_F^2 . \tag{27}$$

To determine the optimal value of B, the objective function that needs to be minimized is

$$\frac{1}{2}\| \tilde{X} - \tilde{X}BA^{\mathrm{T}} \|_F^2 + \alpha\| B \|_1 + \frac{1}{2}\beta\| B \|_F^2 . \tag{28}$$

In the above equation, we set A to A_k and introduce the proximal gradient optimization formula.

$$\nabla B = \tilde{X}^T(\tilde{X}B_k - \tilde{X}A_k) \tag{29}$$

$$B_{k+1} = prox_{\gamma r}(B_k - \gamma\nabla B) \tag{30}$$

Here, $prox_{\gamma r}$ means the proximal operation and γ denotes the learning rate. We solve Eqs. (29) and (30) to obtain A_{k+1} and B_{k+1}, and then substitute these values into Eq. (26) to determine the final optimal sparse load B.

3. Experimental Measurement and Data Mining

3.1 Experimental measurement system

The scaled-down diagram of the gear lubrication system of a nuclear power plant under consideration is shown in Fig. 2(a). The detailed arrangement of the major components of the lubrication pump system is shown in Fig. 2(b). It primarily includes (1) a 5 kW motor, (2) a screw pump, (3) a fan-type cooler, (4) filters, (5) a digital pressure transmitter, (6) a pressure-gauge switch, (7) a vibration-resistant pressure gauge, (8) thermal resistors, (9) bimetal thermometers, (10) check valves, (11) safety valves, (12) throttle valves, and (13) throttle valves.

Our experimental measurement system comprises both hardware and software modules. The hardware module includes the aforementioned lubrication system, sensors, a signal transmission unit, and a signal processing unit, while the software module features a system login function, a monitoring function, and a data logging function.

3.2 Data mining

First, the main failures, known as intermediate events, are divided into four primary categories: insufficient oil-supply pressure, insufficient oil-supply flow, lubricant contamination, and excessively high oil-supply temperature. Each category is directly related to the overall performance and reliability of the lubrication system. We then provide detailed information on all relevant intermediate and basic events in the gear lubrication system, as shown in Table 1.

(a)

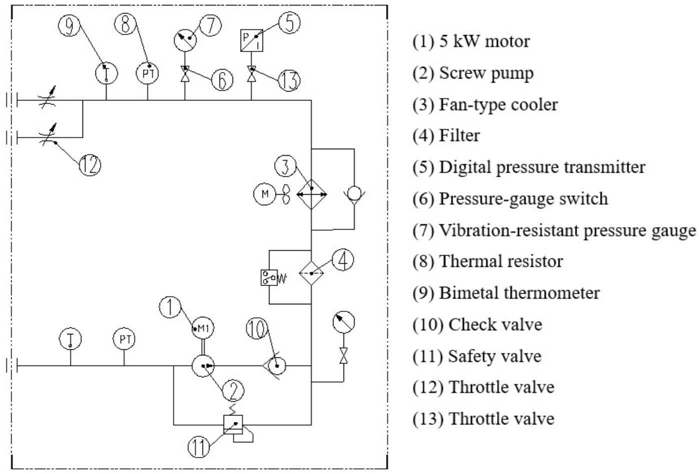

(b)

Fig. 2. (Color online) Scaled-down experimental gear lubrication system of nuclear power plant under consideration.

Table 1
Details of main failures.

No.	Failure type	No.	Failure type
T	Lubrication system failure	X4	Throttle valve damage
M1	Low oil-supply pressure	X5	Fan cooler damage
M2	Insufficient oil-supply flow	X6	Drive motor damage
M3	Lubricant contamination	X7	Heavy wear on pump rotor stator
M4	Excessively high oil-supply temp.	X8	Pipeline leakage
M5	Low supply pressure of oil pump	X9	Oil pump bearing damage
M6	Safety valve failure	X10	Mechanical seal failure of oil pump
M7	Low lubricant viscosity	X11	Filter clogged
M8	Oil pump failure	X12	Fuel tank filter outlet clogged
M9	Excessively high lubricant temperature	X13	Check valve failure
M10	Low pump suction volume	X14	Low set pressure of safety valve
M11	Oil deterioration	X15	Safety valve damage
X1	Insufficient fuel	X16	Throttle over-adjustment
X2	Using wrong grade of lubricant	X17	Filter malfunction
X3	Gear operation overload	X18	Oil aging

Next, on the basis of the above detailed list of events and their logical relationships, we construct the fault tree models, as shown in Figs. 3–7.

The top event (T, lubrication system failure) consists of four main intermediate events (M1–M4), representing the four key dimensions of lubricant supply pressure, lubricant supply flow, lubricant quality, and lubricant temperature, as shown in Fig. 3.

As illustrated in Fig. 4, the low oil-supply pressure (M1) results from issues such as a damaged throttle valve, oil pump failure, or leaks in the piping—each of which might stem from operational errors or equipment damage. As illustrated in Fig. 5, the insufficient oil-supply flow (M2) is caused by a range of fundamental issues, including clogged filters, check valve failure,

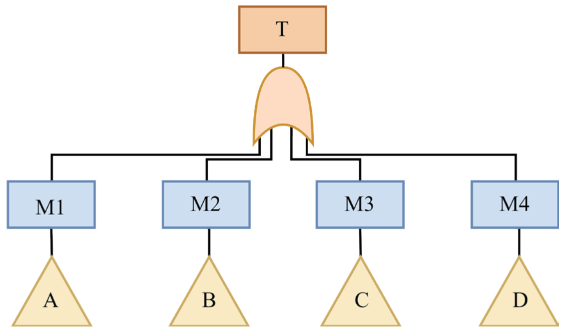

Fig. 3. (Color online) Fault tree of lubrication system failure.

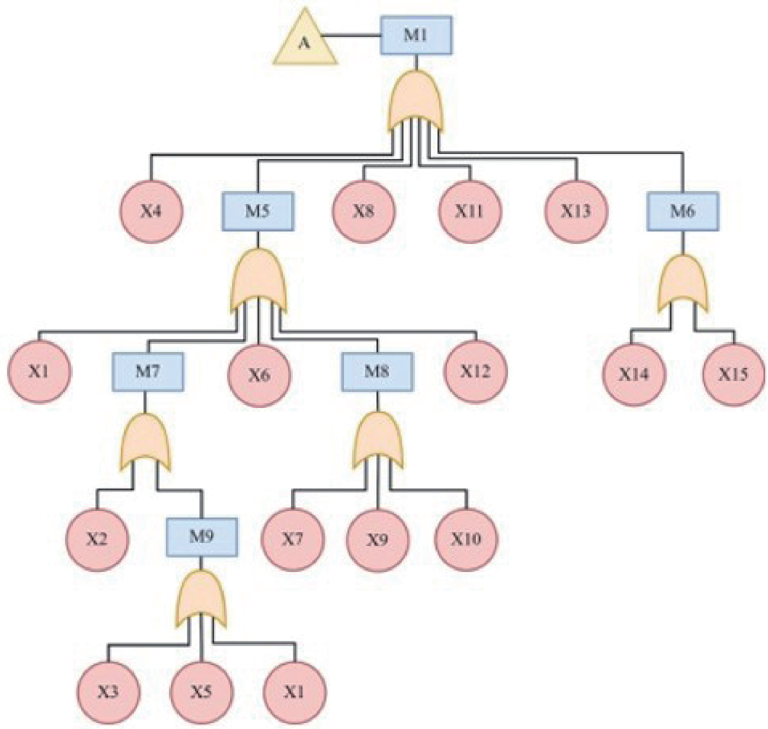

Fast Indexing

M1: Insufficient oil-supply pressure	X1: Insufficient fuel	X7: Heavy wear on pump rotor stator	X13: Check valve failure
M5: Low supply pressure of oil pump	X2: Using wrong grade of lubricant	X8: Pipeline leakage	X14: Low set pressure of safety valve
M6: Safety valve failure	X3: Gear operation overload	X9: Oil pump bearing damage	X15: Safety valve damage
M7: Low lubricant viscosity	X4: Throttle valve damage	X10: Mechanical seal failure of oil pump	
M8: Oil pump failure	X5: Fan cooler damage	X11: Filter clogged	
M9: Excessively high lubricant temperature	X6: Drive motor damage	X12: Fuel tank filter outlet clogged	

Fig. 4. (Color online) Sub-fault tree of insufficient oil-supply pressure.

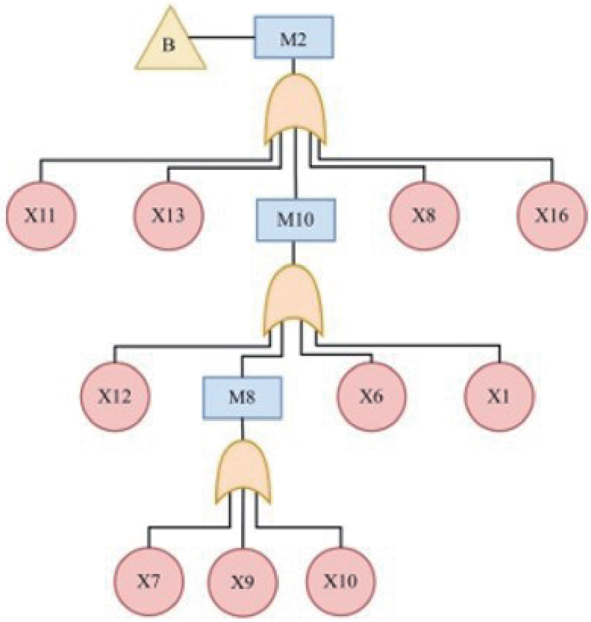

Fast Indexing

M2: Insufficient oil-supply flow	X1: Insufficient fuel	X9: Oil pump bearing damage	X13: Check valve failure
M8: Oil pump failure	X6: Drive motor damage	X10: Mechanical seal failure of oil pump	X16: Throttle over-adjustment
M10: Low pump suction volume	X7: Heavy wear on pump rotor stator	X11: Filter clogged	X17: Filter malfunction
	X8: Pipeline leakage	X12: Fuel tank filter outlet clogged	X18: Oil aging

Fig. 5. (Color online) Sub-fault tree of insufficient oil-supply flow.

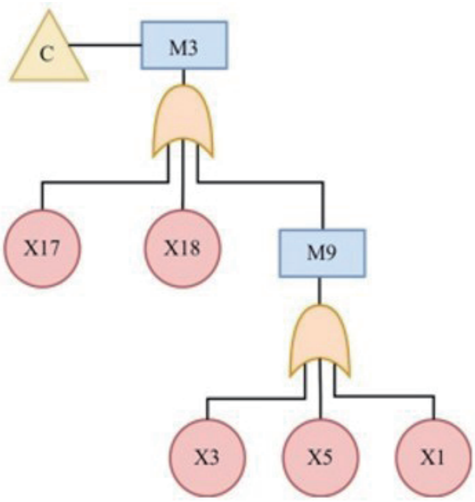

Fast Indexing

M3: Lubricant contamination	X1: Insufficient fuel	X5: Fan cooler damage	X18: Oil aging
M9: Excessively high lubricant temperature	X3: Gear operation overload	X17: Filter malfunction	

Fig. 6. (Color online) Sub-fault tree of lubricant contamination.

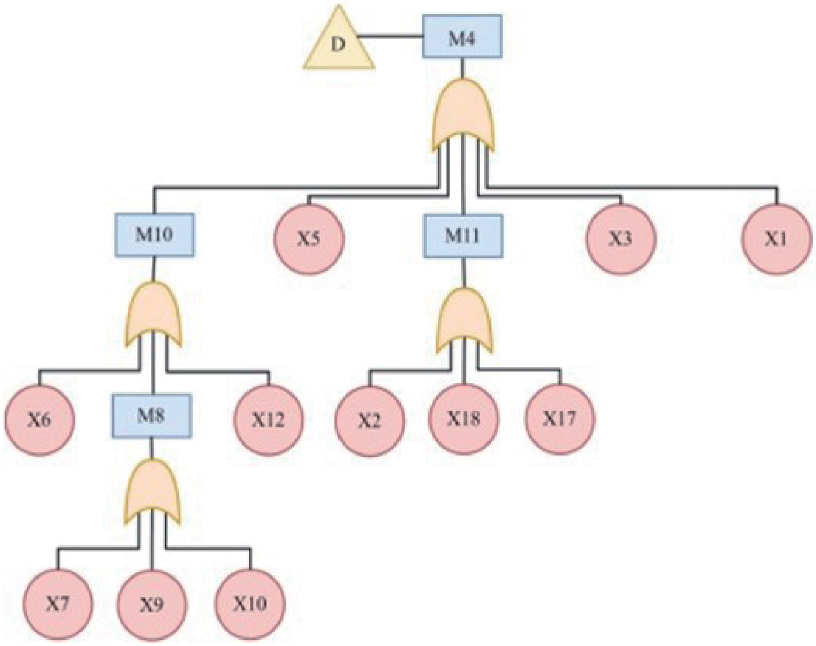

Fast Indexing

M4: Excessively high oil-supply temp.	X1: Insufficient fuel	X6: Drive motor damage	X12: Fuel tank filter outlet clogged
M8: Oil pump failure	X2: Using wrong grade of lubricant	X7: Heavy wear on pump rotor stator	X17: Filter malfunction
M10: Low pump suction volume	X3: Gear operation overload	X9: Oil pump bearing damage	X18: Oil aging
M11: Oil deterioration	X5: Fan cooler damage	X10: Mechanical seal failure of oil pump	

Fig. 7. (Color online) Sub-fault tree of excessively high oil-supply temperature.

and subpar pump performance. As illustrated in Fig. 6, the lubricant contamination (M3) occurs owing to oil deterioration or filter failure, which can be attributed to inadequate maintenance or material degradation. As illustrated in Fig. 7, the high oil-supply temperature (M4) is the result of cooling system malfunctions or the use of an inappropriate lubricant grade, leading to ineffective temperature control.

In the fault tree network, the effects of basic events on intermediate events are interconnected, creating a series of intertwined causal chains. For instance, a basic event such the oil pump bearing damage (X9) has multiple effects, even though it directly leads to the oil pump failure (M8). The failure of the oil pump can lead to low oil-supply pressure (M1), which in turn affects the insufficient oil-supply flow (M2). This chain reaction illustrates the dependence and vulnerability of various components within the lubrication system. Similarly, there are interdependencies and influences among intermediate events. Inadequate oil-supply pressure can directly impact the oil-supply flow, as a malfunctioning oil pump is unable to overcome internal flow resistance to deliver the required amount of oil. Conversely, insufficient oil-supply flow can exacerbate issues such as the low pump suction volume (M10) or the clogged filter (X11), further contributing to low oil-supply pressure (M1).

Additionally, reductions in both oil flow and oil pressure can decrease lubrication efficiency, potentially causing excessively high oil-supply temperatures (M4). Insufficient oil-supply flow (M2) fails to dissipate enough heat, leading to system overheating. Furthermore, the lubricant contamination issues (M3), such as oil aging (X18) and filter malfunctions (X17), can increase wear losses, compromising the efficiency and safety of the lubrication system. This not only affects the oil's lubrication performance, but can also lead to higher oil temperatures, as degraded quality oil may not be able to transfer heat efficiently. In a poorly maintained lubrication system, low-quality oil may exacerbate the negative effects of other basic events such as the overloaded gear operation (X3) and fan cooler damage (X5).

Combining the results of these sub-fault tree analyses reveals recurring basic events that contribute to failures, such as the clogged filter (X11), pipeline leakage (X8), and heavy wear on the pump rotor stator (X7). The presence of these critical events indicates their significant impact on the overall health of the lubrication system.

4. Fault Detection and Diagnosis Algorithms

4.1 Normal and fault state data

First, using the established experimental measurement system (Fig. 2), we measured the lubricant flow parameters—pressure (P, Pa), temperature (T, °C), and volume flow rate (Q, m³/s)—with pressure gauges, thermometers, and velocity sensors under normal operating conditions for a minimum of 12 h. During this period, fluid-flow data were collected every 2 s, resulting in a total of 21600 data points. A portion of these data is shown in Table 2. Through calculations using Eqs. (1)–(15), we obtained the Q and T^2 statistics, which serve as the basis for the

Table 2
(Color online) Portion of measured data of pressure (P, Pa), temperature (T, °C), and volume flow rate (Q, m³/s).

	P1	*P2*	*P3*	*T1*	*T2*	*Q1*	*Q2*
1	0.460	0.480	0.577	32.600	32.767	16.334	14.274
2	0.460	0.480	0.577	32.634	32.767	16.374	14.240
3	0.461	0.480	0.577	32.600	32.767	16.340	14.240
4	0.461	0.479	0.577	32.600	32.734	16.374	14.234
5	0.461	0.479	0.577	32.634	32.767	16.367	14.200
6	0.461	0.480	0.577	32.634	32.767	16.334	14.207
7	0.460	0.480	0.578	32.634	32.767	16.374	14.240
8	0.461	0.479	0.577	32.600	32.800	16.374	14.240
9	0.461	0.480	0.577	32.634	32.800	16.374	14.240
10	0.461	0.480	0.578	32.634	32.767	16.374	14.207
11	0.461	0.479	0.577	32.634	32.767	16.334	14.234
12	0.461	0.480	0.578	32.600	32.767	16.334	14.240
13	0.460	0.479	0.577	32.634	32.767	16.334	14.240
14	0.460	0.479	0.578	32.634	32.767	16.367	14.200
15	0.460	0.479	0.576	32.634	32.800	16.374	14.234
16	0.460	0.479	0.577	32.634	32.800	16.374	14.207
17	0.460	0.479	0.576	32.634	32.767	16.334	14.200
18	0.460	0.478	0.576	32.634	32.767	16.367	14.194
19	0.460	0.479	0.578	32.634	32.767	16.340	14.247
20	0.459	0.478	0.575	32.634	32.800	16.367	14.240

subsequent algorithm training of our proposed data-driven machine learning method. Next, for testing, we created 200 normal-condition data points and 200 fault-condition data points for the gear lubrication system, including cases X7, X8, and X11, resulting in a total of 400 lubricant flow data points. The first 200 data points represent normal-state conditions, while the remaining 200 correspond to fault-state conditions.

4.2 Fault detection of Case X11

The detection results of Case X11 (clogged filter) using the PCA, SPCA, VPPG-SPCA, and VPPGO-ASPCA methods are illustrated in Figs. 8–11, respectively. In these plots, thresholds for the Q and T^2 statistics are indicated by green and red dashed lines, respectively, to differentiate between normal operating and fault states. The fault occurred at the 200th sample, and all samples prior to this point were classified as normal operation. The results indicate that while all four detection methods are generally consistent in their ability to identify faults, they exhibit notable differences in sensitivity and response strength to fault signals. When a fault occurs, both the Q and T^2 statistics increase significantly, although the extent of this increase varies among the different detection algorithms.

From Fig. 11, it can be observed that increasing the weighting factor decreases the mean threshold value. When the pressure difference between the front and rear of the filter exceeds

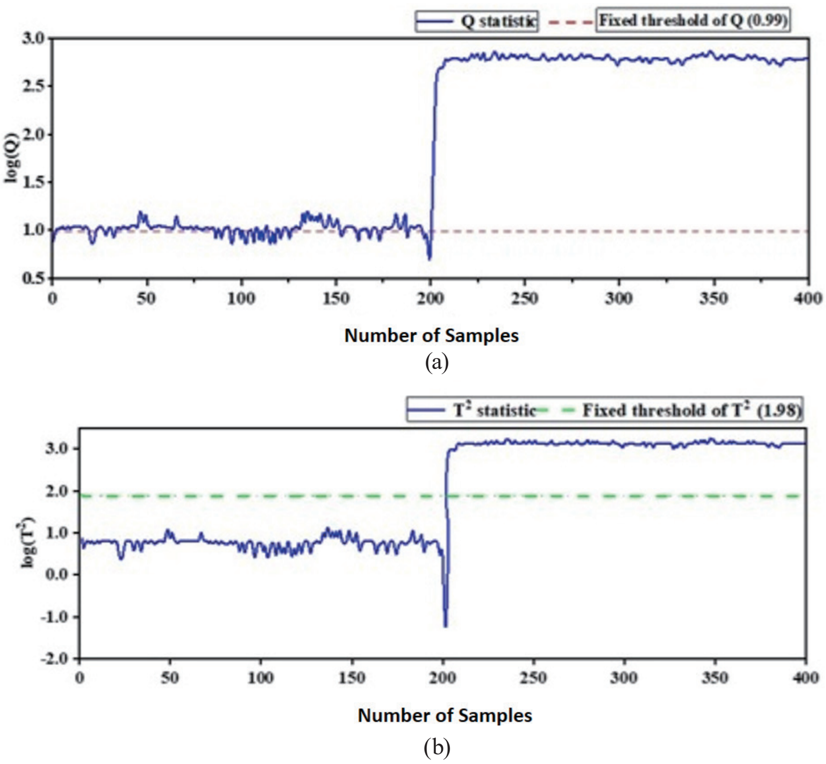

Fig. 8. (Color online) Detection results of Case X11 by PCA method: (a) Q statistic distribution and (b) T^2 statistic distribution.

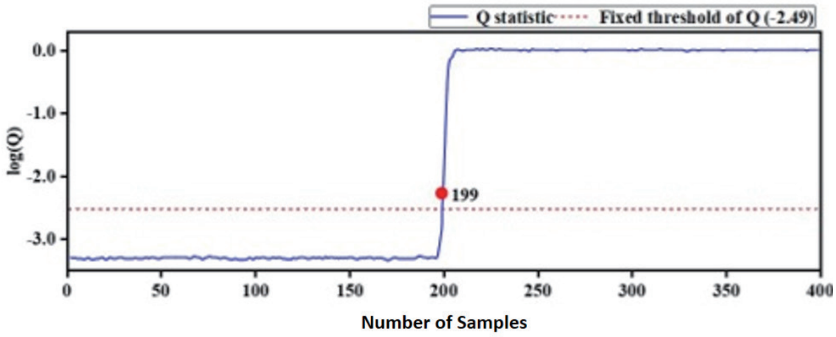

(a)

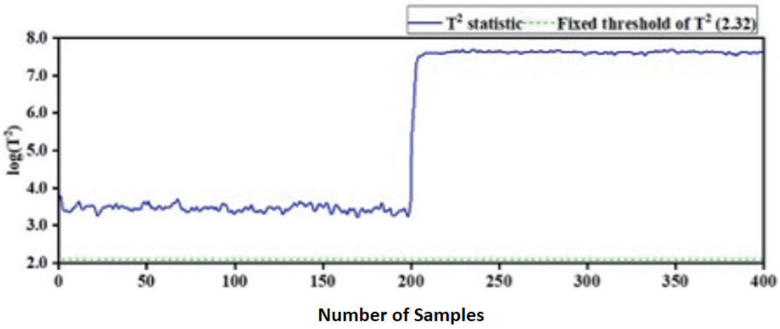

(b)

Fig. 9. (Color online) Detection results of Case X11 by SPCA method: (a) Q statistic distribution and (b) T^2 statistic distribution.

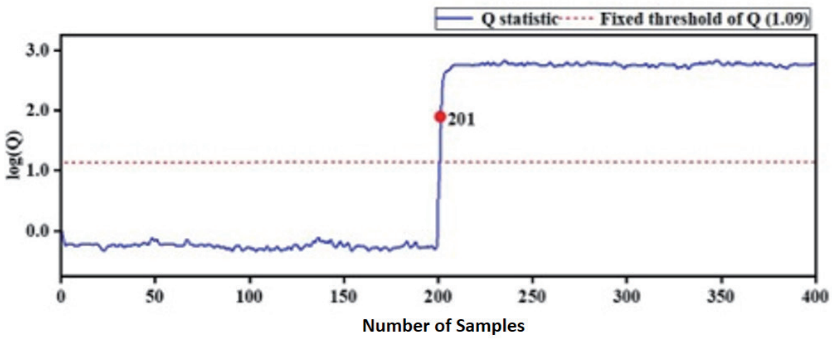

(a)

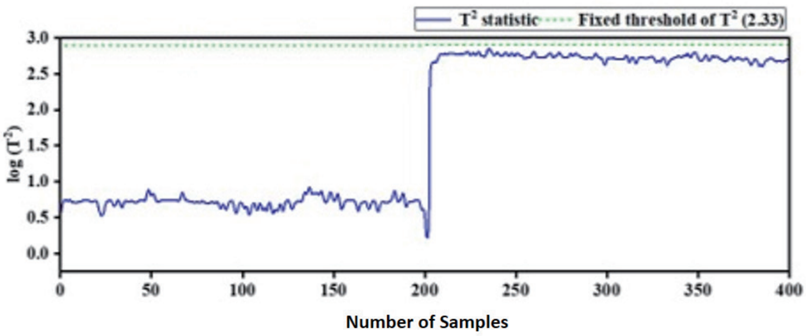

(b)

Fig. 10. (Color online) Detection results of Case X11 by VPPGO-ASPCA method: (a) Q statistic distribution and (b) T^2 statistic distribution.

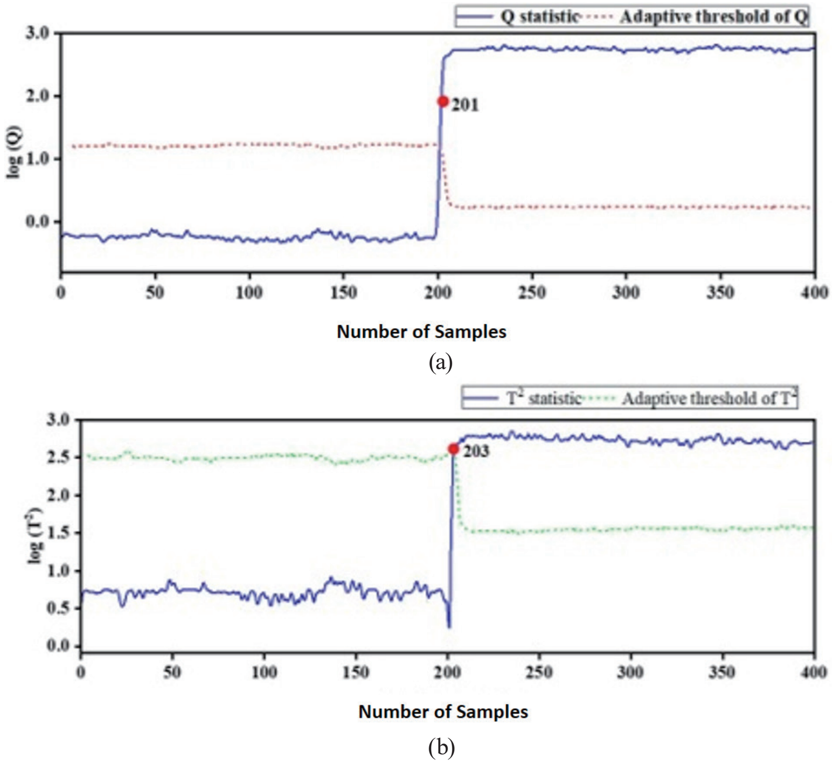

Fig. 11. (Color online) Detection results of Case X11 by VPPGO-ASPCA method: (a) Q statistic distribution and (b) T^2 statistic distribution.

1 MPa, indicating a filter clogging fault, the traditional fixed-threshold method often fails to adjust the threshold value of the T^2 statistic in time, making it difficult to identify the abnormal condition. In contrast, the VPPGO-ASPCA adaptive-threshold method effectively adjusts to changes in T^2 statistic, accurately defining the system's critical state. This adaptive-threshold method significantly enhances the sensitivity and accuracy of system state judgments.

Table 3 shows the comparative results of Q and T^2 statistics obtained using four methods, namely, PCA, SPCA, VPPG-SPCA, and VPPGO-ASPCA, for system fault identification. This includes detection and fault identification rates. The PCA and SPCA methods show excellent fault identification accuracy, approaching 100%. However, the PCA method with the Q statistic as the identification index exhibits a high misidentification rate of 85.5% under normal conditions, whereas SPCA with the T^2 statistic as the identification index has a misidentification rate of 100%. We found that both algorithms, PCA and SPCA, tend to misidentify normal states as faults. In contrast, the VPPG-SPCA algorithm performs moderately well when using the Q statistic for identification, but less effectively with the T^2 statistic. This indicates that VPPG-SPCA is less sensitive to certain fault identification scenarios, particularly in the case of blockage faults. On the other hand, the VPPGO-ASPCA method uses adaptive thresholds for both the T^2 and Q statistics, making it highly sensitive to fault occurrences. This superior sensitivity underscores the effectiveness of the VPPGO-ASPCA method in fault identification.

Table 3
Comparison of various fault detection methods for Case X11.

Methods	PCA		SPCA		VPPG-SPCA		VPPGO-ASPCA	
	Q	T^2	Q	T^2	Q	T^2	Q	T^2
Detection rate (%)	99.5	99.0	100	100	99.5	0	99.5	97.0
Fault identification rate (%)	85.5	0	0.5	100	0	0	0	0

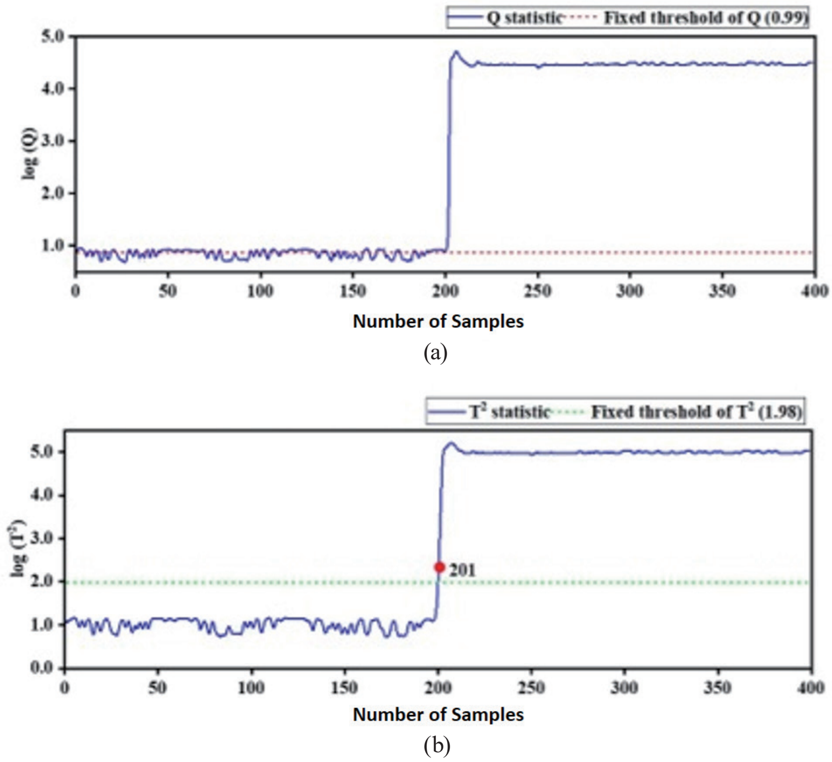

Fig. 12. (Color online) Detection results of Case X8 by PCA method: (a) Q statistic distribution and (b) T^2 statistic distribution.

4.3 Fault detection of Case X8

The detection results of Case X8, using the PCA, SPCA, VPPG-SPCA, and VPPGO-ASPCA methods, are illustrated in Figs. 12–15, respectively. As shown in Fig. 14, the Q and T^2 statistics, which were calculated using the VPPG-SPCA method, demonstrate a high level of identification accuracy for Case X8. This indicates that the relationship between the calculated Q and T^2 statistics and their preset threshold values is appropriate, allowing for the effective detection of fault states. Furthermore, as shown in Fig. 15, the VPPGO-ASPCA method proposed in this study exhibits exceptional fault detection capability for Case X8, particularly when there is a significant discrepancy between the adaptive threshold and the real-time calculated values of the Q and T^2 statistics. This demonstrates that the VPPGO-ASPCA method offers high fault detection sensitivity, a level of performance not attainable with the traditional SPCA model.

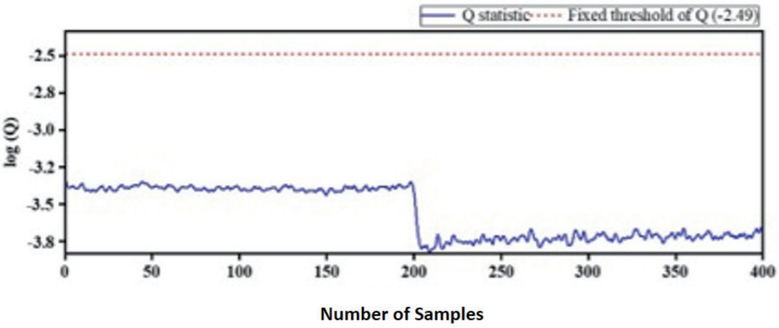

(a)

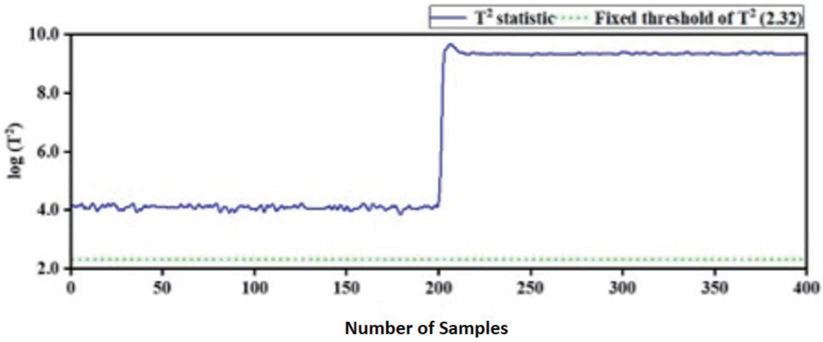

(b)

Fig. 13. (Color online) Detection results of Case X8 by SPCA method: (a) Q statistic distribution and (b) T^2 statistic distribution.

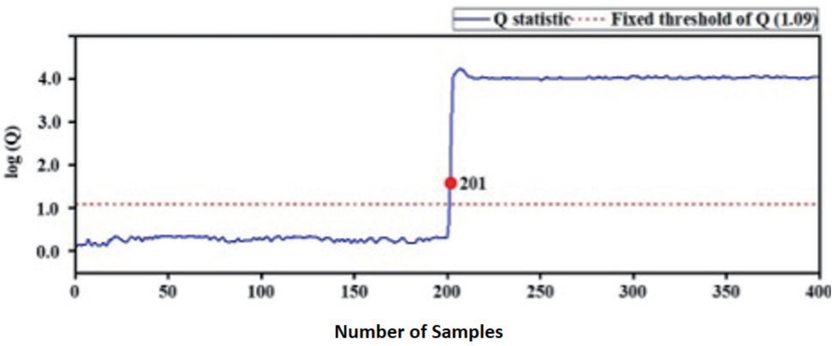

(a)

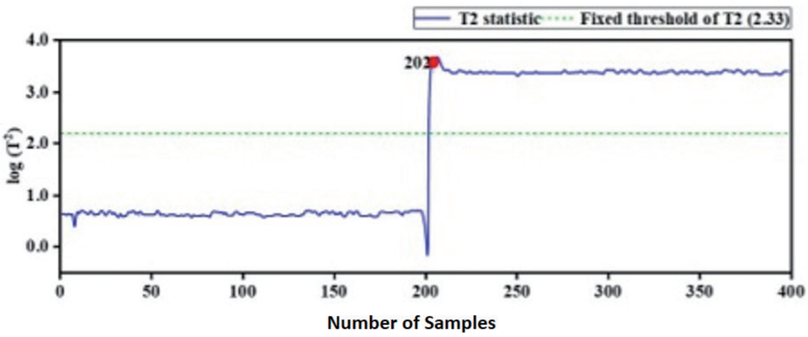

(b)

Fig. 14. (Color online) Detection results of Case X8 by VPPG-SPCA method: (a) Q statistic distribution and (b) T^2 statistic distribution.

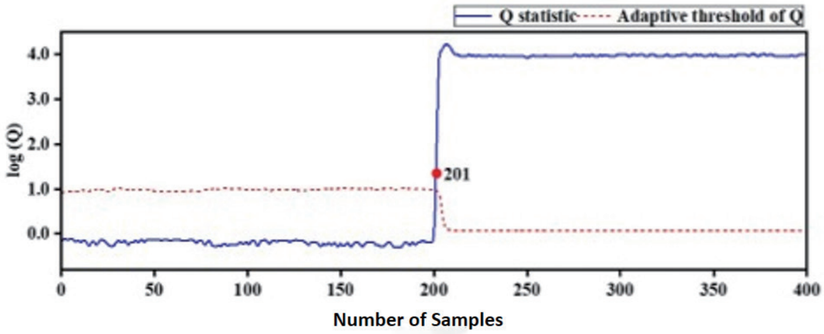

(a)

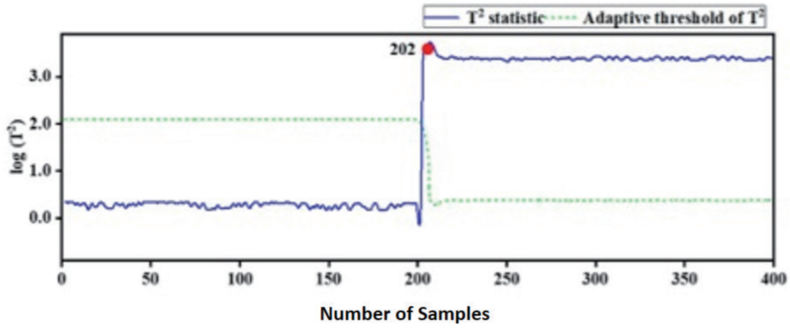

(b)

Fig. 15. (Color online) Detection results of Case X8 by VPPGO-ASPCA method: (a) Q statistic distribution and (b) T^2 statistic distribution.

Table 4 shows a comparison of the test results of the four identification methods for Case X8. The comparison reveals that the PCA method has a false detection rate of 67.0% for normal cases and an even higher rate of 85.5% for the fault case of X8, indicating notably low detection capability. Additionally, the Q statistic distribution calculated by the SPCA method shows a fault detection rate of 0% when faults are present. Thus, both the PCA and SPCA methods demonstrate inadequate identification performance in the event of a fault in the lubrication system. Specifically, the SPCA method, which uses the T^2 statistic, misidentifies all normal cases as failures, likely owing to its oversensitivity to system changes. In contrast, the VPPG-SPCA and VPPGO-ASPCA methods exhibit significantly higher performance in fault detection. The fault detection rate for these two methods exceeds 99%, as indicated by the Q and T^2 statistics. Notably, the adaptive threshold strategy employed by the VPPGO-ASPCA model significantly enhances its adaptability and stability across various operating conditions, making it more reliable in dynamically changing monitoring environments.

4.4 Fault detection of Case X7

We applied the four methods previously mentioned to identify the fault case of X7, with results shown in Figs. 16–19. All four methods successfully detected the fault state of heavy

Table 4
Comparison of the results of various fault detection methods for Case X8.

Method	PCA		SPCA		VP-SPCA		VPPGO-ASPCA	
	Q	T^2	Q	T^2	Q	T^2	Q	T^2
Detection rate (%)	100	99.5	0	100	99.5	99.0	99.5	99.0
Fault identification rate (%)	67.0	0	0	100	0	0	0	0

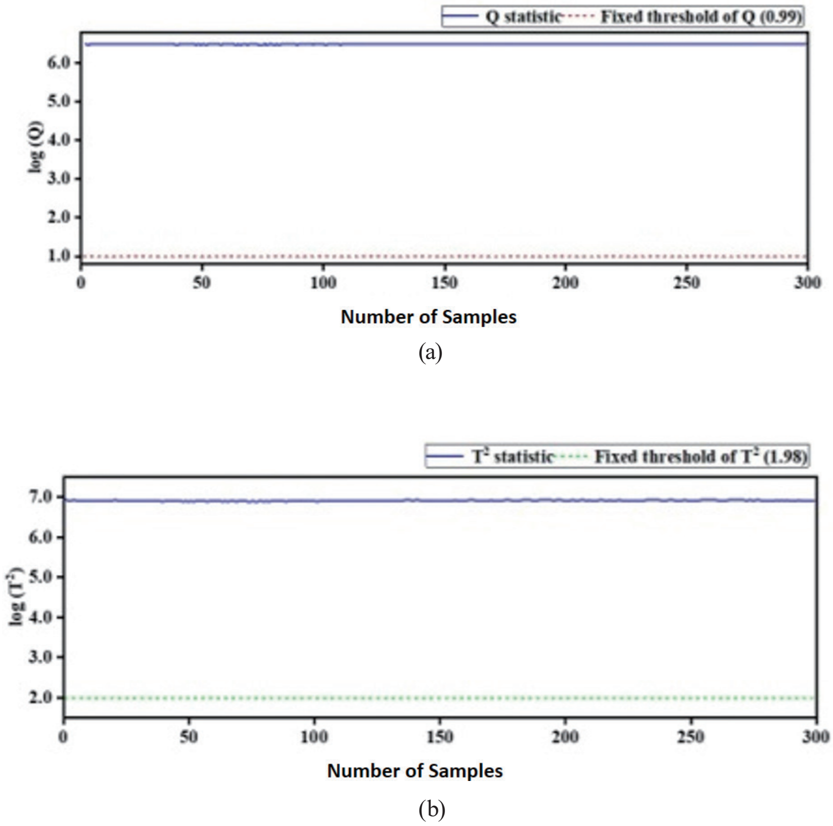

Fig. 16. (Color online) Detection results of Case X7 by PCA method: (a) Q statistic distribution and (b) T^2 statistic distribution.

wear on the pump rotor stator. This success is attributed to the fact that rotor wear has a more pronounced impact on monitoring parameters such as pressure (P) and temperature (T) than other fault conditions.

In summary, the VPPGO-ASPCA fault detection model proposed in this study demonstrates high accuracy across all three fault cases. The model's adaptive threshold technology significantly enhances its ability to identify faults in complex and dynamically changing systems. In contrast, the PCA, SPCA, and VPPG-SPCA models show lower performance in detecting pipeline leakage and filter clogged cases, as evidenced by the substantial variability in the calculated Q and T^2 statistics. This suggests that the PCA, SPCA, and VPPG-SPCA models

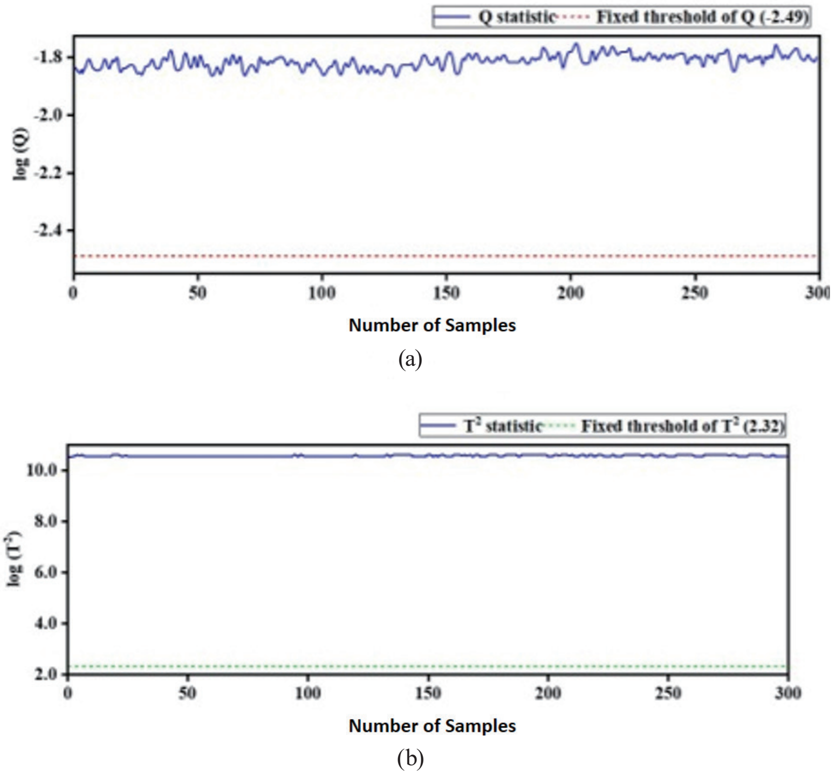

Fig. 17. (Color online) Detection results of Case X7 by SPCA method: (a) Q statistic distribution and (b) T^2 statistic distribution.

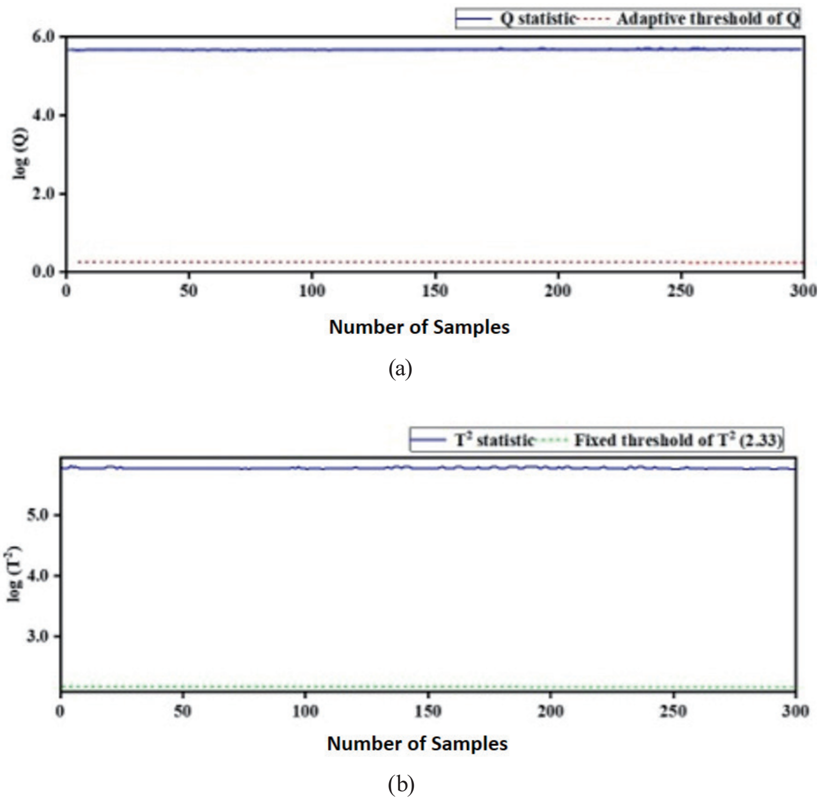

Fig. 18. (Color online) Detection results of Case X7 by VPPG-SPCA method: (a) Q statistic distribution and (b) T^2 statistic distribution.

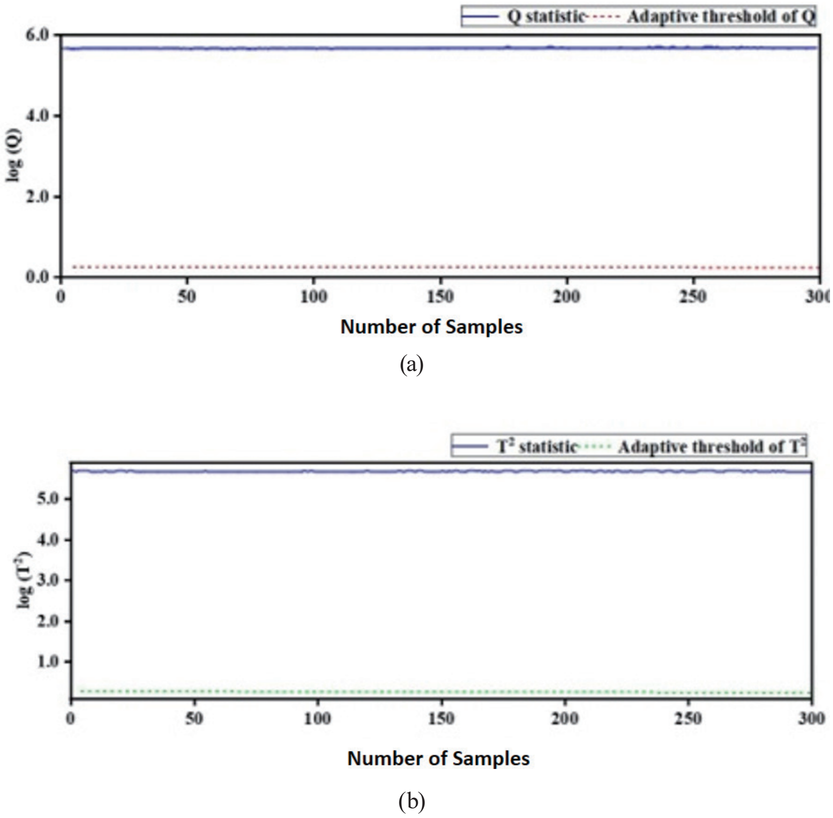

Fig. 19. (Color online) Detection results of Case X7 by VPPGO-ASPCA method: (a) Q statistic distribution and (b) T^2 statistic distribution.

have limitations when handling fault detection in a complex gear lubrication system. In contrast, the VPPGO-ASPCA method overcomes the challenge of setting an effective threshold with limited data through its adaptive technology, ensuring consistent and reliable fault detection across various fault scenarios of a gear lubrication system.

5. Conclusions

Maintaining and monitoring the gear lubrication system of the oil pump is crucial for ensuring safe operation, improving energy efficiency, and extending the equipment life of a nuclear power plant. To address the challenges and issues in fault diagnosis for this gear lubrication system, we proposed a fault detection algorithm of IDDML that combines VPPGO-ASPCA with a fuzzy fault tree. Additionally, we developed a specialized integrated measurement system featuring temperature and pressure sensors to accurately monitor the status of the gear lubrication system. This approach aims to identify various fault conditions effectively. Compared with the traditional internal iteration update method of the SPCA algorithm, the VPPG algorithm rebalances the sparse load update process, significantly enhancing calculation speed. Moreover, the SA threshold in this algorithm addresses the issue of inadequate sensitivity associated with the fixed thresholds of traditional SPCA fault detection methods. Subsequently, with the fault diagnosis of the lubrication system in a nuclear power plant as a case study, experimental results with several high-sensitivity sensors and computations using four network schemes demonstrated that the IDDML fault diagnosis method has outstanding performance, achieving a fault detection rate exceeding 99%. By leveraging this data-driven fault detection and diagnosis algorithm, we successfully achieved intelligent fault detection and diagnosis for the oil pump gear lubrication system of a nuclear power plant.

Acknowledgments

This work was supported by the Program for Key Science and Technology Project of Industry-University-Research Collaborative Innovation in Sanming City, China (Grant No. 2022-G-15), and Sanming University Research Program, China (Grant No. KD24009P), in part by the Major Project of the Fujian STS Program Supporting the Cooperation Between the Academy and the Province (Grant no. 2023T31030123), in part by the Sanming University of Fujian Province, China (Grant Nos. 19YG05 and 19YG04), and in part by the Project of the Department of Education of Fujian Province, China (Grant No. 2022G02010).

References

1 G. Hu, T. Zhou, and Q. Liu: Front. Energy Res. **9** (2021) 663296. https://doi.org/10.3389/fenrg.2021.663296
2 Z. Qiu, X. Yuan, D. Wang, S. Fan, and Q. Wang: Measurement **220** (2023) 113436. https://doi.org/10.1016/j.measurement.2023.113436
3 H. Song, X. Liu, and M. Song: Appl. Energy **341** (2023) 121077. https://doi.org/10.1016/j.apenergy.2023.121077
4 H. Gong, S. Cheng, Z. Chen, and Q. Li: Nucl. Sci. Eng. **196** (2022) 668. https://doi.org/10.1080/00295639.2021.2014752
5 Y. Shi, X. Xue, Y. Qu, and J. Xue: 2021 Int. Conf. Data Mining Workshops (ICDMW) Auckland, New Zealand (IEEE, 2021) 917.
6 G. Wu, Z. Duan, D. Yuan, and J. Yin: Front. Energy Res. **9** (2021) 665502. https://doi.org/10.3389/fenrg.2021.665502
7 X. Zhao, X. Wang, and M. W. Golay: Nucl. Technol. **209** (2023) 401. https://doi.org/10.1080/00295450.2022.2142445
8 A. Ayodeji, Y. Liu, and H. Xia: Prog. Nucl. Energy **105** (2018) 42. https://doi.org/10.1016/j.pnucene.2017.12.013
9 G. Wu, D. Yuan, J. Yin, Y. Xiao, and D. Ji: Front. Energy Res. **9** (2021) 641545. https://doi.org/10.3389/fenrg.2021.641545
10 J. A. Farber and D. G. Cole: Prog. Nucl. Energy **128** (2020) 103469. https://doi.org/10.1016/j.pnucene.2020.103469
11 H. Wang, M. Peng, Y. Yu, H. Saeed, C. Hao, and Y. Liu: Ann. Nucl. Energy **150** (2021) 107786. https://doi.org/10.1016/j.anucene.2020.107786
12 W. Li, M. Peng, and Q. Wang: Ann. Nucl. Energy **119** (2018) 342. https://doi.org/10.1016/j.anucene.2018.05.024
13 L. Chao, C. Wang, S. Chen, Q. Duan, and H. Xie: Sci. Technol. Nucl. Install. **11** (2022) 1. https://doi.org/10.1155/2022/2675875
14 J. Ling, G. Liu, J. Li, and X. Shen: Nucl. Sci. Tech. **31** (2020) 75. https://doi.org/10.1007/s41365-020-00792-9
15 L. Ren, W. Lv, S. Jiang, and Y. Xiao: IEEE Trans. Instrum. Meas. **65** (2016) 2313. https://doi.org/10.1109/TIM.2016.2575318
16 A. Pawashe, S. S. Kalkundri, C. Chavan, and R. Arunachalam: 2017 Int. Conf. Microelectron. Devices, Circuits and Systems (ICMDCS) (2017) 1. https://doi.org/10.1109/ICMDCS.2017.8211690
17 D. Ren, H. Zeng, X. Wang X, and S. Pang: 2020 6th Int. Conf. Control, Automation and Robotics (ICCAR) (2020) 423. https://doi.org/10.1109/ICCAR49639.2020.9108107
18 Y. Wang, T. Cui, F. Zhang, and T. Dong: 2016 Int. Conf. Control, Automation and Information Sciences (ICCAIS) (2016) 221. https://doi.org/10.1109/ICCAIS.2016.7822464
19 J. Wang, Z. Wang, F. Gu, X. Ma, J. Fei, and Y. Cao: Advances in Asset Management and Condition Monitoring, A. Ball, L. Gelman, and B. K. N. Rao, Eds. (Springer, Cham) **166** (2019) 573. https://doi.org/10.1007/978-3-030-57745-2_48

20 B. Liu, Q. Yang, X. Wu, S. Fang, and F. Guo: Int. J. Plant Eng. Manage. **22** (2017) 12. https://doi.org/10.13434/j.cnki.1007-4546.2017.0102
21 C. Joshi, F. Ruggeri, and S. P. Wilson: IEEE Trans. Reliab. **67** (2018) 170. https://doi.org/10.1109/TR.2017.2778241
22 G. Li, C. Xiong, J. Gao, H. Zhu, C. Wang, and J. Xiao: J. Build. Eng. **82** (2024) 108230. https://doi.org/10.1016/j.jobe.2023.108230.
23 A. J. Vickers: BMC Med. Res. Methodol. **5** (2005) 35. https://doi.org/10.1186/1471-2288-5-35
24 P. Peng, Y. Zhang, F. Liu, H. Wang, and H. Zhang: IEEE Access **7** (2019) 133799. https://doi.org/10.1109/ACCESS.2019.2928329
25 L. Luo, S. Bao, and C. Tong: Ind. Eng. Chem. Res. **58** (2019) 1300. https://doi.org/10.1021/acs.iecr.8b04655
26 Y. Wang and Y. Han: Math. Probl. Eng. **2022** (2022) 1. https://doi.org/10.1155/2022/1406676
27 Z. Geng, X. Duan, Y. Han, F. Liu, and W. Xu: ISA Trans. **128** (2022) 21. https://doi.org/10.1016/j.isatra.2021.11.002.
28 H. Zou, T. Hastie, and R. Tibshirani: J. Comput. Graphical Stat. **15** (2006) 265. https://doi.org/10.1198/106186006X113430
29 Y. Fu, C. Luo, and X. Xu: Ind. Eng. Chem. Res. **63** (2024) 5803. https://doi.org/10.1021/acs.iecr.3c04244